TECHNICAL ARTICLE

Deformation Behavior, Microstructure Evolution and Hot Workability of an Extruded Mg-2Y-0.5Zn-0.5Ni Alloy

Jing Jiang, Haobin Xu, Yashuo Wang, Guangli Bi, Yuandong Li, and Tijun Chen

Deformation behavior, microstructure and hot workability of an extruded Mg-2Y-0.5Zn-0.5Ni (MYZN, at.%) alloy were investigated in the temperature range of RT $\sim$ 300 °C and strain rate range of 0.01– $1 \times 10^{-4} \ s^{-1}$. Besides α-Mg, $Mg_{24}Y_5$ and Mg_2Y, three kinds of LPSO phases appeared in the extruded MYZN alloy, the lamellar 18R-LPSO phase, the massive 18R-LPSO phase and the thin strip 14H-LPSO phase and stacking faults (SFs) distributed in the grain interior. The tensile tests indicated that the tensile strengths of the alloy decreased, while the elongation increased gradually with increasing temperature and decreasing strain rate. At 300 °C with a strain rate of $4 \times 10^{-4} \ s^{-1}$, the extruded alloy indicated a quasi-superplasticity with an elongation of 130.3%. The extruded alloy exhibited a dislocation slipping at lower temperatures (< 200 °C) with different strain rates, while grain boundary sliding assisted dislocation slipping at 300 °C. Also, the optimum processing window is 247–300 °C/4×10^{-4}–$1 \times 10^{-3} \ s^{-1}$.

1. Introduction

In recent years, Mg alloys, as one of the most promising lightweight metal materials, have attained more attention due to their low density, high specific strength and good electromagnetic shielding and easy to recycle. Parts of them has been widely used in automobile, aerospace and 3C industries (Ref 1, 2). However, the poor room-temperature workability arose from their *hcp* structure with few slip systems, which remarkably limits their developments and application. Thus, it is necessary to investigate the deformation behavior of Mg alloy to expend their application fields. Recently, Mg-RE (rare earth)-TM (transition metal) alloys exhibit excellent mechanical properties at both room and elevated temperatures (Ref 3-6). In order to further meet the requirements of engineering applications, it is particularly important to improve the plastic forming properties of Mg alloys, especially at room temperature. It is reported that the properties of LPSO phase would affect the mechanical properties, deformation behavior and hot workability of the alloy, such as size, morphology, amounts and structure type (Ref 6, 7). Zhang et al. (Ref 8) studied the microstructure and mechanical properties of the extruded Mg-2Y-Cu-TM (TM = Cu, Zn, Co, Ni) alloys. The lamellar or massive LPSO phase appears to be in a more fragmented and dispersed state after extrusion results in the better mechanical properties of the alloy by the LPSO phase strengthening. Li et al. (Ref 9) investigated the influence of high-density lamellar LPSO phases on the deformation behavior of the extruded Mg-5.6Gd-0.8Zn (wt.%) alloy. The results indicate that the kink of the LPSO phase could coordinate the uniform deformation of the alloy. Luo et al. (Ref 10) also pointed out that the Mg-5Y-3Ni-0.2Zr alloy contained more LPSO phases with kink angle shows the high mechanical properties as compared with Mg-5Y-3Zn-0.2Zr (wt.%) alloy, suggesting that the LPSO phase has a good ability to accommodate the deformation. Bi et al. (Ref 11) systematically investigated the deformation behavior of the extruded Mg-2Dy-0.5Zn (at.%) alloy under an uniaxial tensile test at RT $\sim$ 300 °C and strain rates ranging from $3 \times 10^{-5} \ s^{-1} \sim 3 \times 10^{-1} \ s^{-1}$. The results indicate that grain boundary (GB) sliding dominates the whole deformation behavior at 300 °C with low strain rates, while dislocation slipping is main deformation mechanism at low temperatures (RT $\sim$ 200 °C) with different strain rates. Recently, Zhang et al. (Ref 12) investigated the deformation behavior of the extruded Mg-5Zn-2.5Y-1Ce-0.5Mn alloy at RT $\sim$ 350 °C with strain rate of $1 \times 10^{-2} \ s^{-1}$–$4 \times 10^{-4} \ s^{-1}$ and revealed that the deformation mechanism changes from dislocation slip at RT to dislocation climb at 250 °C and to GB sliding at 350 °C. Yang et al. (Ref 13) studied the deformation behavior of the extruded Mg-5Gd-3Y-(1,2)Zn-0.5Zr alloy at different temperatures (RT $\sim$ 300 °C) and confirmed that the basal and non-basal slip cooperatively dominate the deformation of both alloys at 100 °C and that gradually becomes dominant with the increase in temperature.

Additionally, the effects of the above properties of LPSO phase on the workability of Mg alloys have been reported. Jin et al. (Ref 14) investigated the workability of Mg-3.7Gd-2.9Y-0.7Zn-0.7Zr through compression tests at temperatures of 375-475 °C and strain rate range of 0.1-1 s^{-1}, and the corresponding processing diagram indicated that the optimum processing window is 415-435 °C/0.001-0.006 s^{-1} and 435-475 °C/0.01-1 s^{-1}. Zhou et al. (Ref 15) demonstrated that the hot

Jing Jiang, Haobin Xu, Yashuo Wang, Guangli Bi, Yuandong Li, and **Tijun Chen,** State Key Laboratory of Advanced Processing and Recycling of Nonferrous Metals, Lanzhou University of Technology, Lanzhou 730050, China; and School of Material Science and Engineering, Lanzhou University of Technology, Lanzhou 730050, China. Contact e-mails: Jiangjing6101@163.com and glbi@163.com.

workability of the Mg-Y$_{2x}$-Zn$_x$ (x = 1, 0.5 and 0.25 at.%) alloy is significantly improved by increasing the amount of block LPSO phase by Zn alloying. Therefore, the systematic research on the hot deformation behavior and workability of Mg alloys under different conditions is not only beneficial to improve the formability of Mg alloys, but also to reasonably design the hot working process. At present, the effects of LPSO phase on the deformation behavior and workability of Mg alloys are not entirely clear and the corresponding relation of the processing window and microstructure is need to be further elucidated during different conditions. Moreover, based on our previous investigation (Ref 16), the addition of single Ni could increase the volume fraction of LPSO phase, while the composite addition of Zn and Ni to Mg-Y alloy could simultaneously improve strength and ductility of the extruded Mg-2Y-0.5Zn-0.5Ni (at.%) alloy; however, the deformation behavior and hot workability of the alloy have not been reported. So, in this paper, we investigated the deformation behavior, microstructure evolution and hot workability of the alloy, which would provide a theoretical basis for extending the application of Mg alloys in production and life.

2. Experimental Procedures

The experimental Mg-2Y-0.5Zn-0.5Ni (MYZN) alloy was prepared by pure Mg (99.99%), pure Zn (99.99%), pure Mg-20Ni (wt.%) and Mg-20Y (wt.%) master alloy. The alloy was melted in a resistance furnace under an anti-oxidizing flux at 750 °C. Subsequently, the melts were homogenized at 720 °C for 30 min after stirring for 10 min and then cast into a cylindrical ingot (Φ = 90 mm, L = 500 mm) through a water-cooling steel mold (Ref 16). The ingot was extruded into a sheet with a cross section of 40 mm × 10 mm after homogenizing at 400 °C for 12 h in a box-type resistance furnace. The extrusion temperature, extrusion ratio and extrusion speed were 366 °C, 16:1 and 0.5 m s^{-1}, respectively. In order to prevent the recrystallization of the extruded alloy, the extruded sheet was immediately cooled using tap water.

Microstructure and phase structure of the extruded alloy were characterized by laser confocal microscope (OM, LSM800), x-ray diffraction (XRD, Rigaku D/max 2500 PC), scanning electron microscope (SEM, Quanta Feg 450) and transmission electron microscope (TEM, FEI Talos F200X). Samples for OM and SEM observation were ground with 200#, 400#, 600#, 800# and 1000# sandpaper, polished and then etched for $\sim$ 30 s in picric acid solution (2.75 g picric acid, 45 mL alcohol, 2.5 mL acetic acid and 5 mL distilled water) and 2% HNO$_3$ alcohol solution. The sample for TEM observation was mechanically polished and thinned by ion beam to $\sim$ 5 μm thickness and processed a thin foil with diameter of 3 μm through a puncher. The average grain size of the alloy was measured by a linear intercept method, and the volume fraction of precipitates and dynamically recrystallized grains was analyzed by using an Image J software. Analysis and characterization of high-resolution TEM (HRTEM) image and the corresponding fast Fourier transform (FFT) were conducted using digital micrograph (DM), and the dislocation density was obtained by calculating the number of dislocation lines across a unit cross-sectional area.

Tensile testing was carried out on a universal tensile testing machine (Instron 1211) at room temperature (RT), 100 °C, 200 °C and 300 °C with strain rates of 1 × 10^{-2} s^{-1}, 3 × 10^{-3} s^{-1}, 1 × 10^{-3} s^{-1} and 4 × 10^{-4} s^{-1}, respectively. Tensile specimens with a gauge dimension of 43 mm × 8 mm × 1.5 mm were cut from the extruded sheet along extrusion direction (ED) using a wire cut electrical discharge machining (DK7732). To ensure the accuracy of data, each parameter needed to be measured at least three times. During high-temperature tensile experiment, the tensile samples were heated to the target temperature and held for 5 min to achieve uniform temperature. The detailed schematic diagram of high-temperature tensile testing was shown in Fig. 1.

3. Results and Discussion

3.1 Microstructure

Figure 2 shows the OM and SEM microstructures of the extruded MYZN alloy, and the horizontal direction of the image is the ED. As shown in Fig. 2(a) and (b), the alloy consists of deformed grains and recrystallized grains after extrusion. It can be seen that the grain of the extruded alloy is obviously refined due to the dynamic recrystallization (DRX). The average grain size of the extruded MYZN is $\sim$ 1.79 μm. In addition, the second phase is also obviously fragmented and distributes along the ED. The volume fraction of the second phase in the extruded MYZN alloy is about 36.2%. As shown in Fig. 2(c) and (d), the LPSO phase of the alloy presents three kinds of morphologies, namely blocky LPSO phase, lamellar LPSO phase distributed along the grain boundary as well as fine stripe-like phase in the grain interior. According to our previous experimental results (Ref 16), the block and lamellar phases are 18R-LPSO phase and the strip-like phase is 14H-LPSO phase with small amounts of stacking faults (SF). Figure 3 shows the corresponding XRD patterns of the extruded alloy. In addition to the LPSO phase, the diffraction peaks of Mg$_2$Y phase are also observed in Fig. 3, while those of Mg$_{24}$Y$_5$ phase and rich Y phase are not reflected in XRD patterns due to their small amounts.

The morphology and distribution of LPSO phase affects DRX of the alloy during extrusion. The fine block 18R-LPSO phase at the grain boundary could effectively promote DRX through the particle-stimulated nucleation (PSN) mechanism (Ref 17, 18). In contrast, the fine stripe-like 14H-LPSO phase inside the grain inhibits the occurrence of DRX, because the limited space between the 14H-LPSO phase and α-Mg matrix does not allow dislocations to reaggregate to form sub-grain boundaries, even though parts of dislocations tend to aggregate at the interface between two phases (Ref 19).

3.2 Tensile Properties

Figure 4 shows the mechanical properties $vs.$ strain rate curves of the extruded MYZN alloy at different temperatures and the corresponding mechanical properties are listed in Table 1. It can be seen from Fig. 4(a) that the ultimate tensile strength (σ_{UTS}) and yield strength ($\sigma_{0.2}$) of the extruded alloy increase, whereas the elongation (ε_f) decreases with increasing strain rate and decreasing temperature. For example, as the strain rate is 4 × 10^{-4} s^{-1} at room temperature (RT), the $\sigma_{0.2}$, σ_{UTS} and ε_f of the extruded alloy are 327 MPa, 357 MPa and 18.1%, respectively. In contrast, as the strain rate is 1 × 10^{-2} s^{-1}, the $\sigma_{0.2}$, σ_{UTS} and ε_f of the extruded alloy increase by
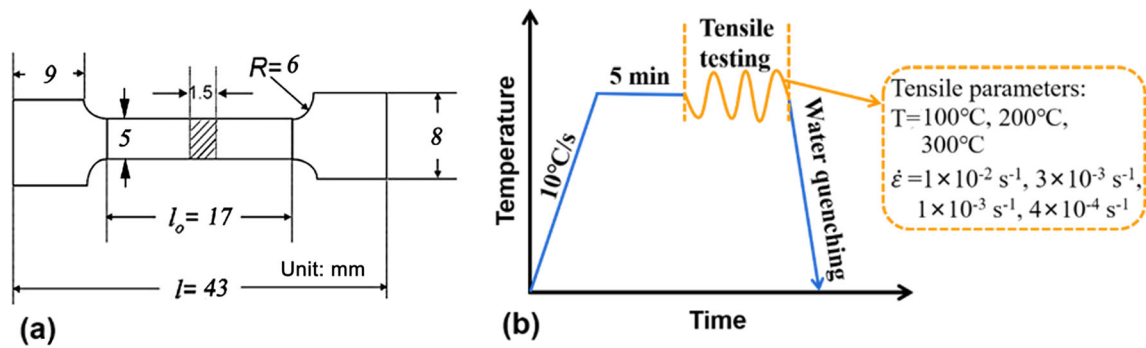
Fig. 1 (a) Schematic diagram of the tensile sample for the extruded MYZN alloy; (b) heat treatment schematic diagram of high-temperature tensile testing
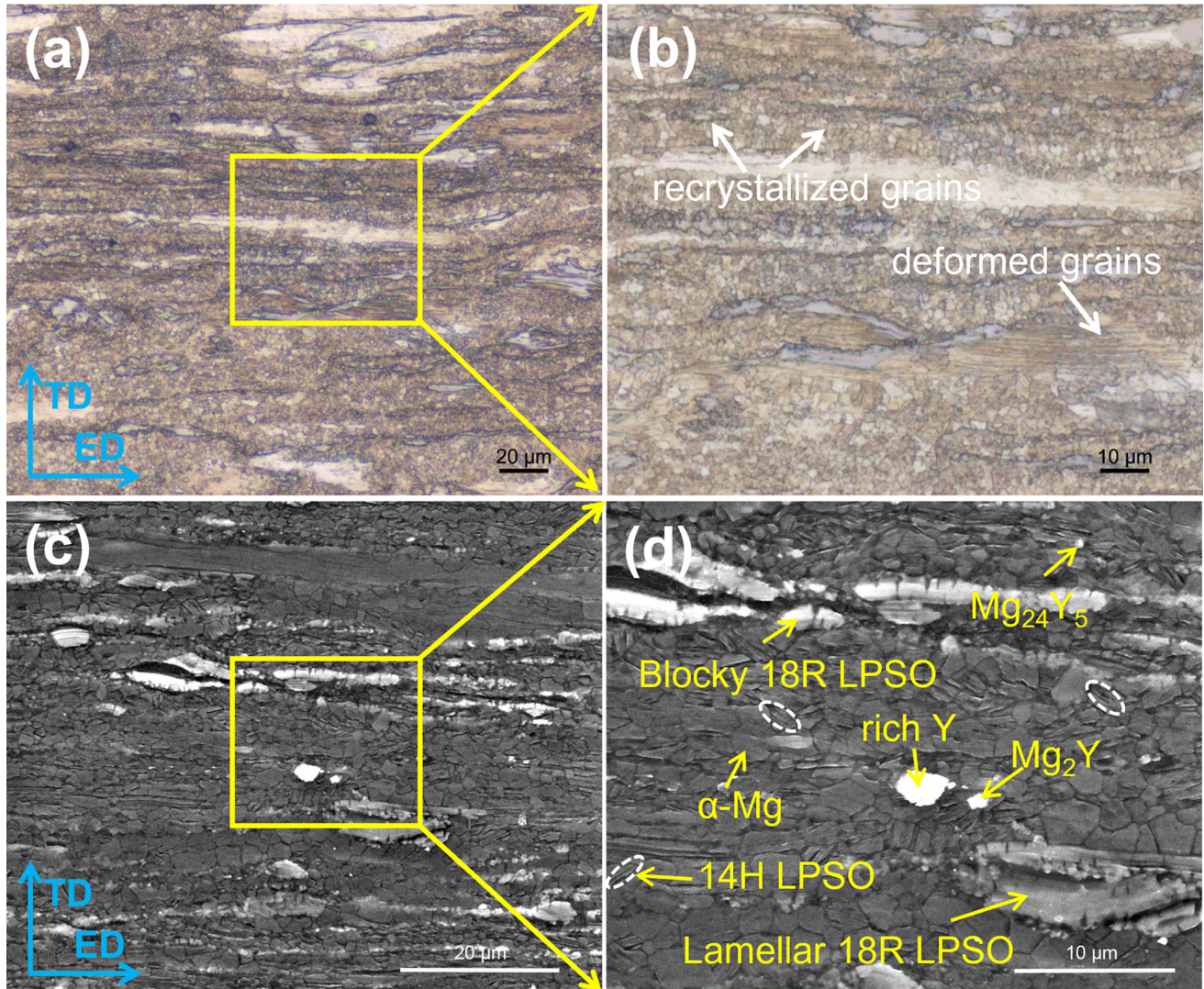

Fig. 2 Microstructures of the extruded MYZN alloy: (a), (b) OM; (c), (d) SEM

5.2% (344 MPa), 10.6% (395 MPa), while ε_f decreases by 11.8% (16.2%), respectively. When the strain rate is 4×10^{-4} at 300 °C, the $\sigma_{0.2}$, σ_{UTS} and ε_f of the extruded alloy are 142 MPa, 158 MPa and 130.3%, respectively. For $\dot{\varepsilon} = 1 \times 10^{-2}\ s^{-1}$, the $\sigma_{0.2}$, σ_{UTS} of the extruded alloy increase by 55.0% and 49.4%, while the ε_f decreases by 67.4%, respectively. It can

be seen that the variation of tensile properties with strain rate of the extruded alloy at high temperatures is more significant than that at RT as seen in Fig. 4(c).

In order to further understand the deformation behavior of the extruded MYZN alloy at various temperatures and strain rates, the true stress–strain curves of the extruded MYZN alloy
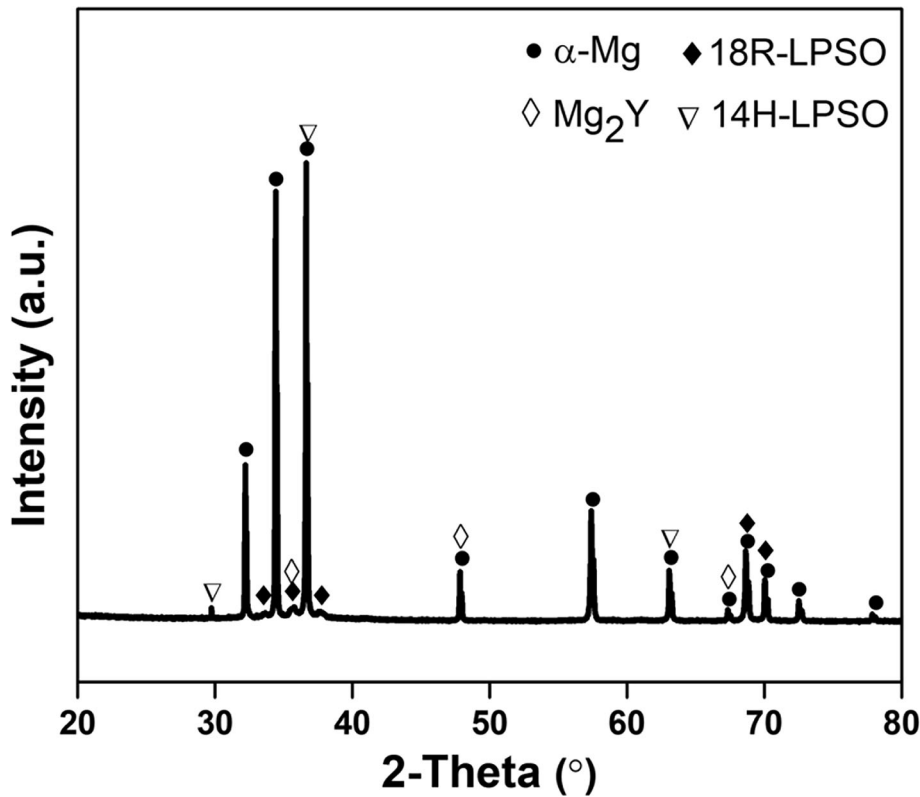
Fig. 3 XRD patterns of the extruded MYZN alloy

are shown in Fig. 5. The strain rate sensitivity coefficient (m) of the alloy is calculated according to following Eq 1:

$$m = \frac{\partial \log \sigma}{\partial \log \dot{\varepsilon}} \qquad (Eq\ 1)$$

where $\dot{\varepsilon}$ and σ are the strain rate and flow stress, respectively. Figure 6 shows the relationship between strain rate and flow stress of the extruded MYZN alloy at different temperatures when the strain is 0.05. It can be found from Fig. 6 that the slope of curve is m value by fitting calculation, whose value increases with increasing testing temperature. The m value of the extruded alloy at 300 °C is 0.17, which is an order of magnitude higher than that of the alloy at RT ($m = 0.03$), 100 °C ($m = 0.04$) and 200 °C ($m = 0.05$). It has been reported that m value determines the deformation mechanism of the alloy, i.e., m < 0.1, dislocation slip and twinning are main deformation mechanism of the alloy (Ref 20); 0.1 < m < 0.5, grain boundary sliding accompanied with dislocation slip controls the whole deformation of the alloy (Ref 6); $m \geq 0.5$, grain boundary sliding, grain rotation and grain boundary diffusion are main deformation mechanism of the alloy (Ref 21, 22). Therefore, it can be inferred that there are two kinds of deformation mechanisms for the present alloy based on the detailed m value range at different temperatures. That is, the alloy appears a dislocation slip at low temperatures (RT < T < 200 °C) with different strain rates, while that does grain boundary sliding accompanied with dislocation slip at 300 °C under same strain rate. The lateral surface observation of tensile specimens after fracturing at different temperatures and strain rates also further confirms this result.

To further reveal the elevated deformation mechanism of the alloy, the constitutive equation is used to calculate the deformation activation energy (Q) of the alloy:

$$\sigma = K \varepsilon^n \dot{\varepsilon}^m \exp\left(\frac{Q}{RT}\right) \qquad (Eq\ 2)$$

where ε is the strain, K is the constant, $\dot{\varepsilon}$ is the strain rate, σ is the flow stress, m is the strain rate sensitive coefficient, and n is the stress index, which is equal to the reciprocal of m, Q is the deformation activation energy of the alloy, T is the absolute temperature, R is the gas constant ($R = 8.314$ J/ (mol·K)). In order to obtain the relation of Q, Eq 2 can be transformed in to Eq 3:

$$\dot{\varepsilon} = K' \sigma^{1/m} \exp\left(\frac{Q}{RT}\right) \qquad (Eq\ 3)$$

We can get Eq 4 by taking log of both side of Eq 3, as following:

$$\ln \sigma = m\frac{Q}{RT} + m\ln\left(\frac{\dot{\varepsilon}}{K'}\right) \qquad (Eq\ 4)$$

Therefore, when $\dot{\varepsilon}$ and m are constant, ln σ and $1/T$ are used as variables, and Eq 5 can be obtained:

$$\frac{\partial \ln \sigma}{\partial (1/T)} = \frac{mQ}{R} \qquad (Eq\ 5)$$

It can be seen that the slope of lnσ and $1/T$ is related to the Q value, which can be obtained by following Eq 6:

$$Q = \frac{R}{m} \cdot \frac{\partial \ln \sigma}{\partial (1/T)} \qquad (Eq\ 6)$$
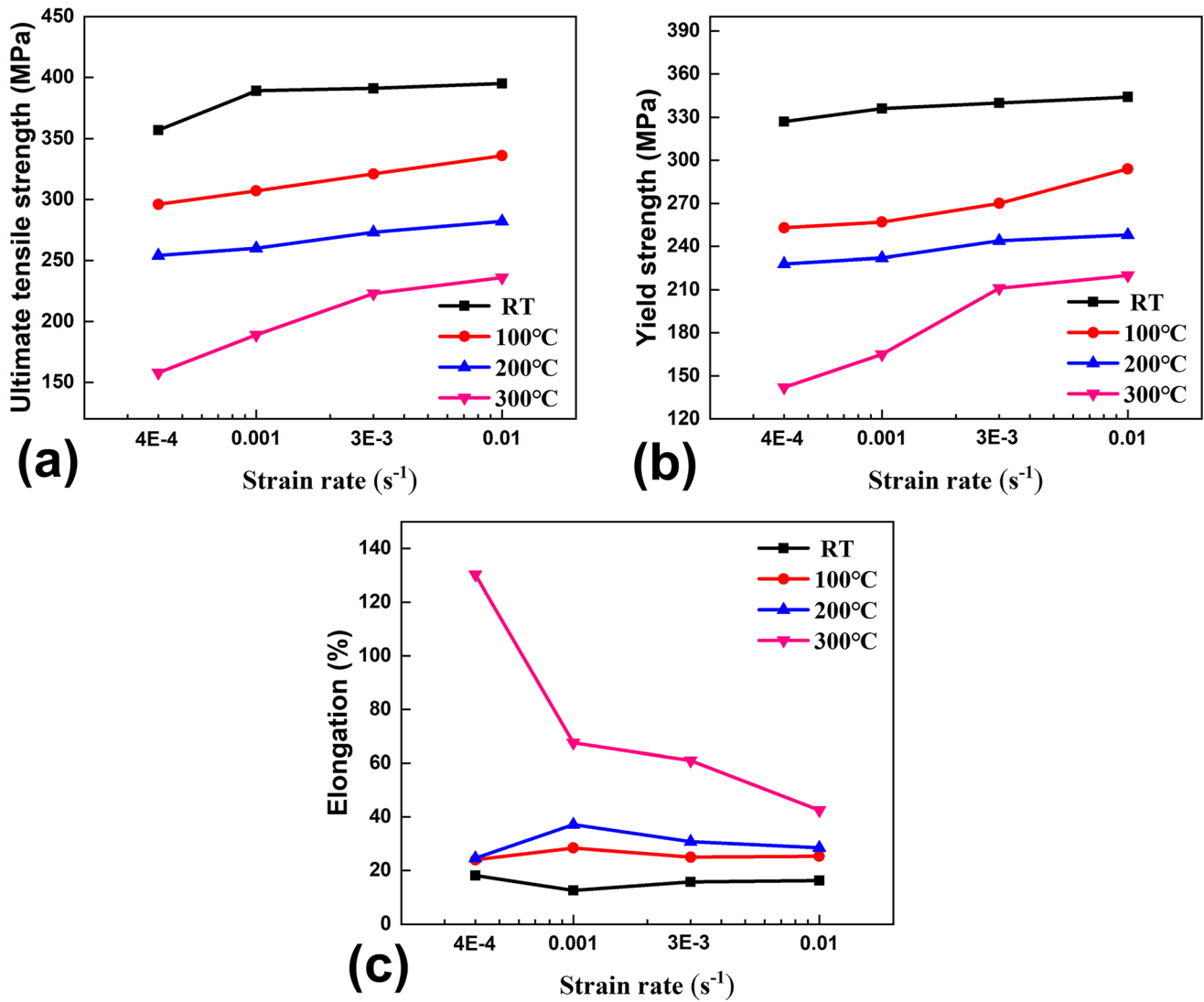
Fig. 4 Mechanical properties vs strain rate curves of extruded MYZN alloy at different temperatures: (a) ultimate tensile strength, (b) yield strength and (c) elongation to failure

Table 1 Tensile properties of the extruded MYZN alloy at different temperatures and strain rates

T, °C	$\dot{\varepsilon}$ s^{-1}	σ_{UTS}, MPa	σ_{TYS}, MPa	ε_f, %
RT	1×10^{-2}	395	344	16.2
	3×10^{-3}	391	340	15.7
	1×10^{-3}	389	336	12.6
	4×10^{-4}	357	327	18.1
100	1×10^{-2}	336	294	25.3
	3×10^{-3}	321	270	25.0
	1×10^{-3}	307	257	28.4
	4×10^{-4}	296	253	24.0
200	1×10^{-2}	282	248	28.5
	3×10^{-3}	273	244	30.8
	1×10^{-3}	260	232	37.1
	4×10^{-4}	254	228	24.6
300	1×10^{-2}	236	220	42.5
	3×10^{-3}	223	211	61.0
	1×10^{-3}	189	165	67.6
	4×10^{-4}	158	142	130.3

According to above equations of (3)-(6), the linear relation curve between Q and $\dot{\varepsilon}$ is shown in Fig. 7. At 300 °C with strain rate of 1×10^{-2} s^{-1} and 4×10^{-4} s^{-1}, the Q of the alloy is 103.87 kJ/mol and 132.05 kJ/mol, respectively. It is found that the Q value of the alloy at 300 °C with high strain rates is close to the activation energy of grain boundary diffusion (95 kJ/mol) (Ref 23), while that of the alloy at 300 °C with low strain rates is closer to the lattice diffusion activation energy (135 kJ/mol) (Ref 24, 25), indicating that the GB sliding accommodated by lattice diffusion controls the main deformation at this condition.

3.3 The Hot Processing Map

In the hot working process of metal, how to choose the processing temperature and deformation rate is very important for the application of this metal in practical life. Therefore, the hot processing map based on dynamic material model (DMM) came into being (Ref 26). The model is used to describe the relationship between deformation parameters and thermal workability of the alloy at high temperatures. The hot
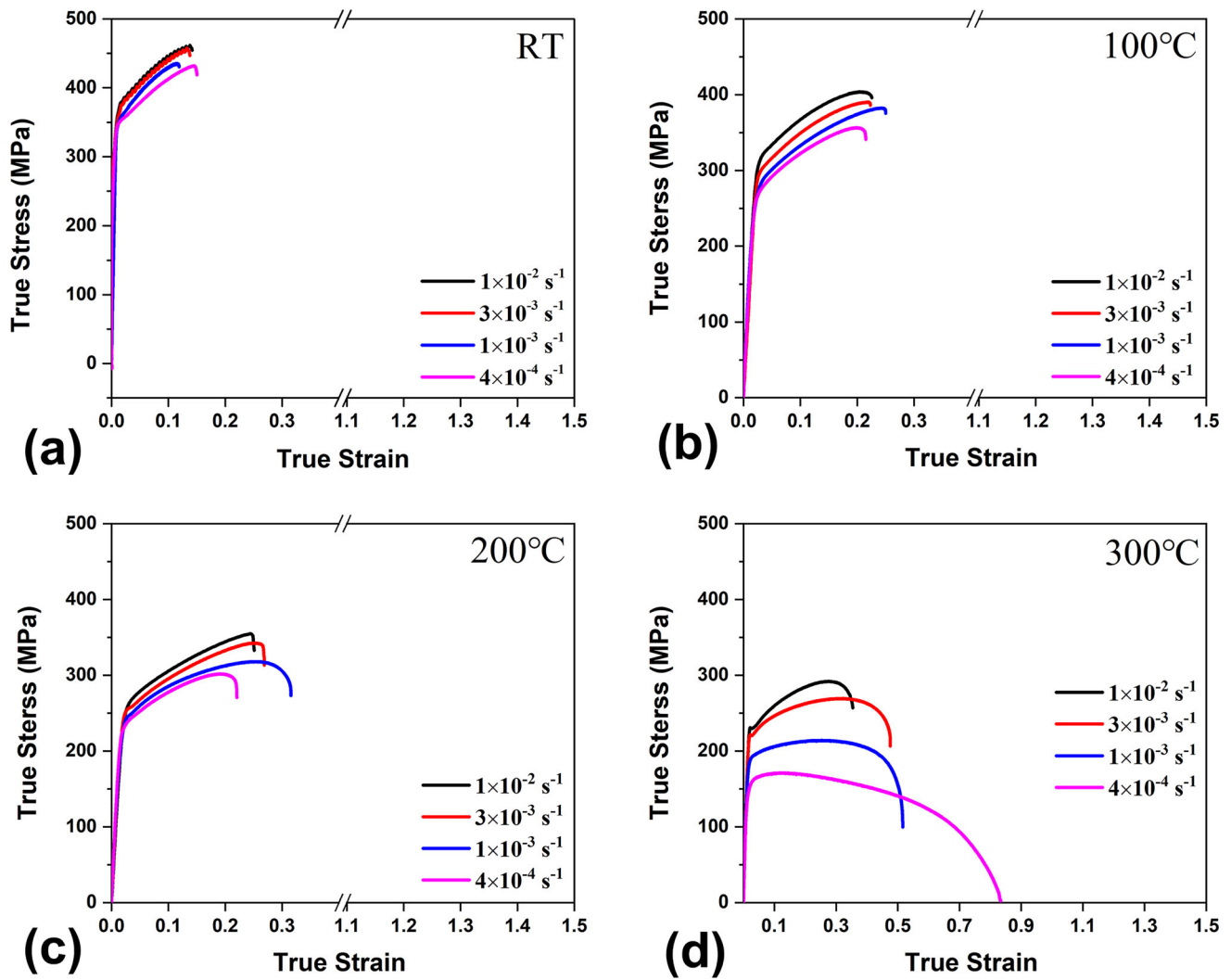
Fig. 5 True stress–strain curves of the extruded MYZN alloy at different temperatures and strain rates

processing map is mainly divided into two parts: energy dissipation diagram and instability diagram. Firstly, based on the m value at a strain of 0.05 according to Eq 1, the energy dissipation coefficient, η, can be obtained by substituting the value of m into Eq 7 below:

$$\eta = \frac{2m}{m+1} \qquad (Eq\ 7)$$

The instability criterion could be defined by Eq 8:

$$\xi(\dot{\varepsilon}) = \frac{\partial \ln\left(\frac{m}{m+1}\right)}{\partial \ln\varepsilon} + m < 0 \qquad (Eq\ 8)$$

The calculated m, η and the instability criterion, ξ, of the extruded MYZN alloy under different deformation conditions are shown in Tables 2, 3 and 4, respectively. The obtained η and ξ values are used to draw the corresponding energy dissipation diagram and instability diagram and finally are superposed to form a hot processing map, as shown in Fig. 8. The value of contour line in Fig. 8 represents the energy dissipation rate. In generally, the processing performance of materials is determined by energy dissipation rate and instability criterion. Under

the condition that stability is guaranteed, the higher the energy dissipation rate, the more suitable the material is for processing in this region (Ref 27). In this work, the white regions with high η values, Regions I and II as marked pink in Fig. 8, are the flow stability of the extruded MYZN alloy. It is found that with the increase in processing temperature, the energy dissipation rate also gradually increases. Region II (247-300 °C/4 × 10⁻⁴-1 × 10⁻³ s⁻¹) has the higher energy dissipation coefficients (14.7-31.8%) than that (5-8.6%) of Region I (64-222 °C/4 × 10⁻⁴-1 × 10⁻² s⁻¹). The typical microstructures of the extruded MYZN alloy at 200 °C/1 × 10⁻² s⁻¹ (Region I) and 300 °C/4 × 10⁻⁴ s⁻¹ (Region II) as shown in Fig. 13(b) and (f) indicate the degree of DRX of Region II is the higher than that of Region I. In addition, the limited grain growth and a great number of uniform microcavities (see Fig. 12(k) and 13(f)) also shows the extruded MYZN alloy exhibits a good plasticity in Region II. Therefore, Region II is identified as the suitable processing window for the extruded MYZN alloy.

In contrast, the red regions marked by A (25–64 °C/4 × 10⁻⁴–1 × 10⁻² s⁻¹) and B (183–247 °C/4 × 10⁻⁴–2 × 10⁻³ s⁻¹ and 222–300 °C/1 × 10⁻³–1 × 10⁻² s⁻¹) in Fig. 8 represent the flow instability of the extruded MYZN alloy during hot
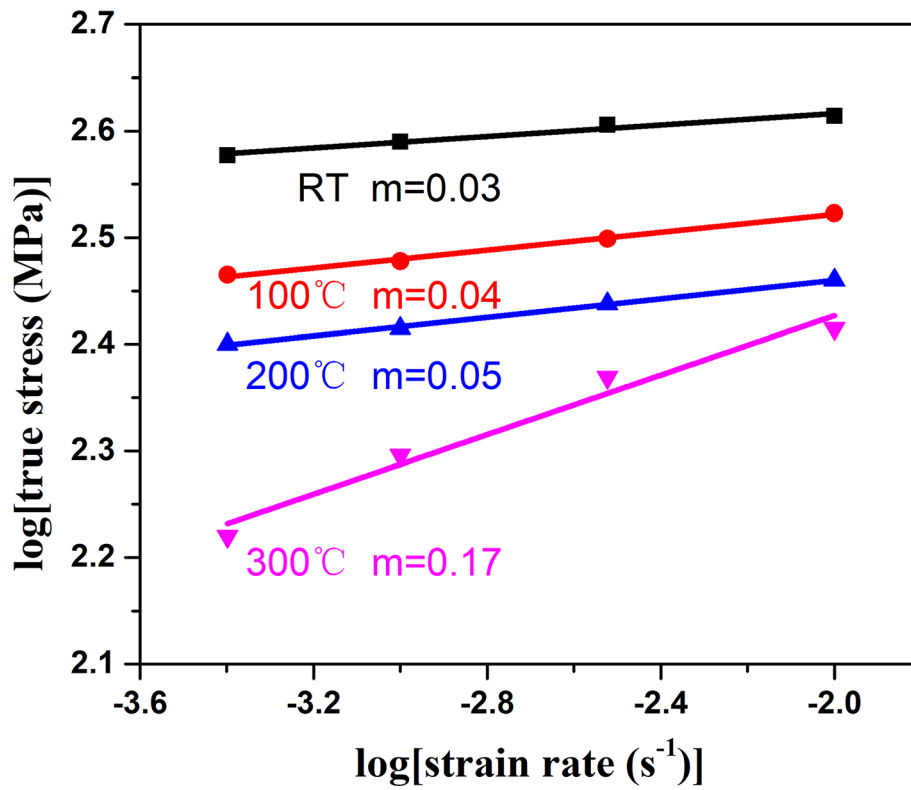
Fig. 6 Variation of logσ and log $\dot{\varepsilon}$ at a true strain of 0.05 for extruded MYZN alloy at different temperatures
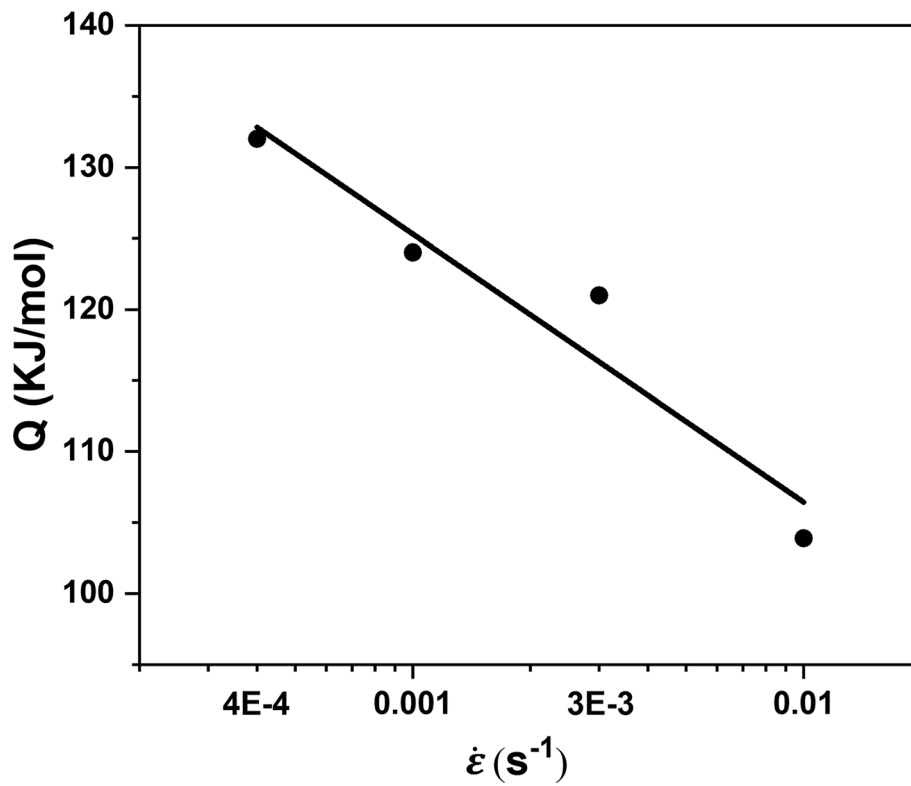

Fig. 7 Variation of Q value with strain rate of the extruded MYZN alloy at 300 °C

Table 2 The strain rate sensitivity coefficient (m) of extruded MYZN alloy at different temperatures and strain rates

$\dot{\varepsilon}$, s^{-1}	RT	100, °C	200, °C	300, °C
4×10^{-4}	0.026	0.035	0.033	0.164
1×10^{-3}	0.020	0.039	0.030	0.189
3×10^{-3}	0.013	0.044	0.030	0.083
1×10^{-2}	0.012	0.045	0.032	0.026

Table 3 The energy dissipation coefficient (η) of the extruded MYZN alloy at different temperatures and strain rates

$\dot{\varepsilon}$, s^{-1}	RT	100, °C	200, °C	300, °C
4×10^{-4}	0.050	0.067	0.064	0.282
1×10^{-3}	0.040	0.075	0.058	0.318
3×10^{-3}	0.026	0.085	0.057	0.153
1×10^{-2}	0.023	0.086	0.062	0.051

Table 4 The instability criterion (ξ) of the extruded MYZN alloy at different deformation conditions

$\dot{\varepsilon}$, s^{-1}	RT	100, °C	200, °C	300, °C
4×10^{-4}	$-$ 0.235	0.160	$-$ 0.066	0.296
1×10^{-3}	$-$ 0.300	0.156	$-$ 0.026	$-$ 0.079
3×10^{-3}	$-$ 0.222	0.106	0.056	$-$ 0.706
1×10^{-2}	$-$ 0.080	0.059	0.098	$-$ 0.883

deformation, in which the ξ values are negative. For instability A and B (183–247 °C/4×10^{-4}–2×10^{-3} s^{-1}) regions, it can be concluded from the typical microstructures of fracture regions of tensile specimens (Fig. 13a, d and e) that the insufficient DRX occurs in low temperatures with different strain rates, which leads to uneven deformation and the appearance of the flow instability (Ref 14). For instability B (222–300 °C/1×10^{-3}–1×10^{-2} s^{-1}) region, the high temperature and high strain rate would yield a large amount of heat at the center of the tensile specimen in the short time, which is difficult to rapidly diffuse and finally results in a local plastic deformation and thus instability (Ref 28). These factors would lead to the adverse effects on mechanical properties. Therefore, the processing in these unstable regions should be avoided as far as possible.

3.4 Fracture Analysis and Surface Observation

Figure 9 shows the macroscopic morphologies of tensile samples of the extruded MYZN alloy before and after fracture. It can be seen from Fig. 9(a) and (b) that the size of the tensile sample after stretching does not change significantly as compared with that of unstretched sample, and there is no obvious necking at the fracture with decreasing strain rates at RT and 100 °C. This indicates that the elongation of the alloy is not affected by the strain rate, which is consistent with the tensile results in Fig. 4(c). As shown in Fig. 9(c) and (d), the samples after stretching show a slight necking phenomenon, especially at 200 °C with low strain rates (1×10^{-3} s^{-1} and 4×10^{-4} s^{-1}), while does an obvious necking at 300 °C with different strain rates. Here, the above macroscopic morphologies and surface observation of tensile specimens at 100 °C are similar to those at RT, so we just focus on analyzing the deformation behavior of tensile samples at RT, 200 °C and 300 °C.
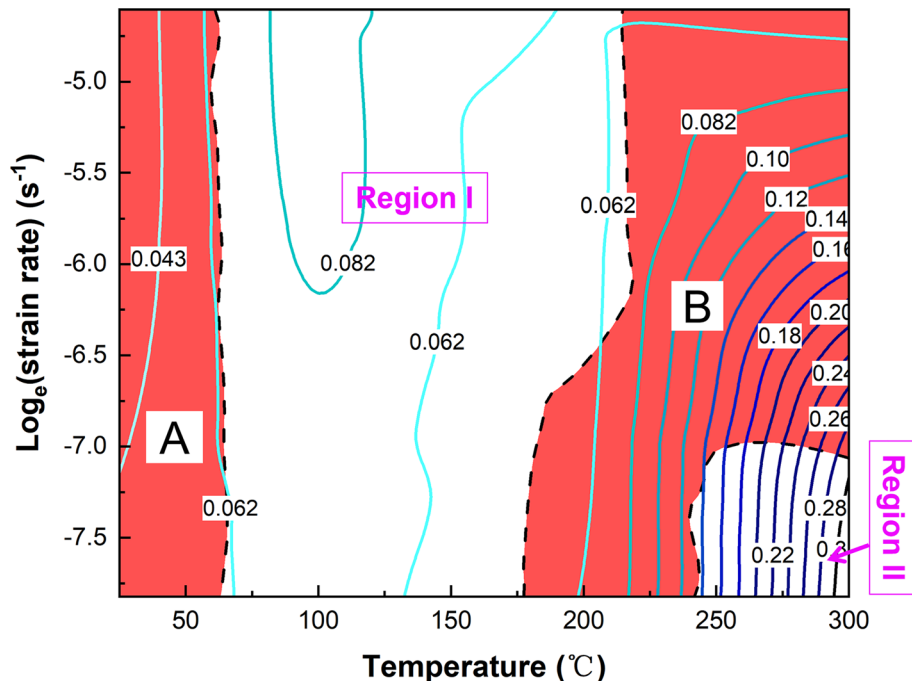

Fig. 8 DMM processing map of the extruded MYZN alloy at a strain of 0.05
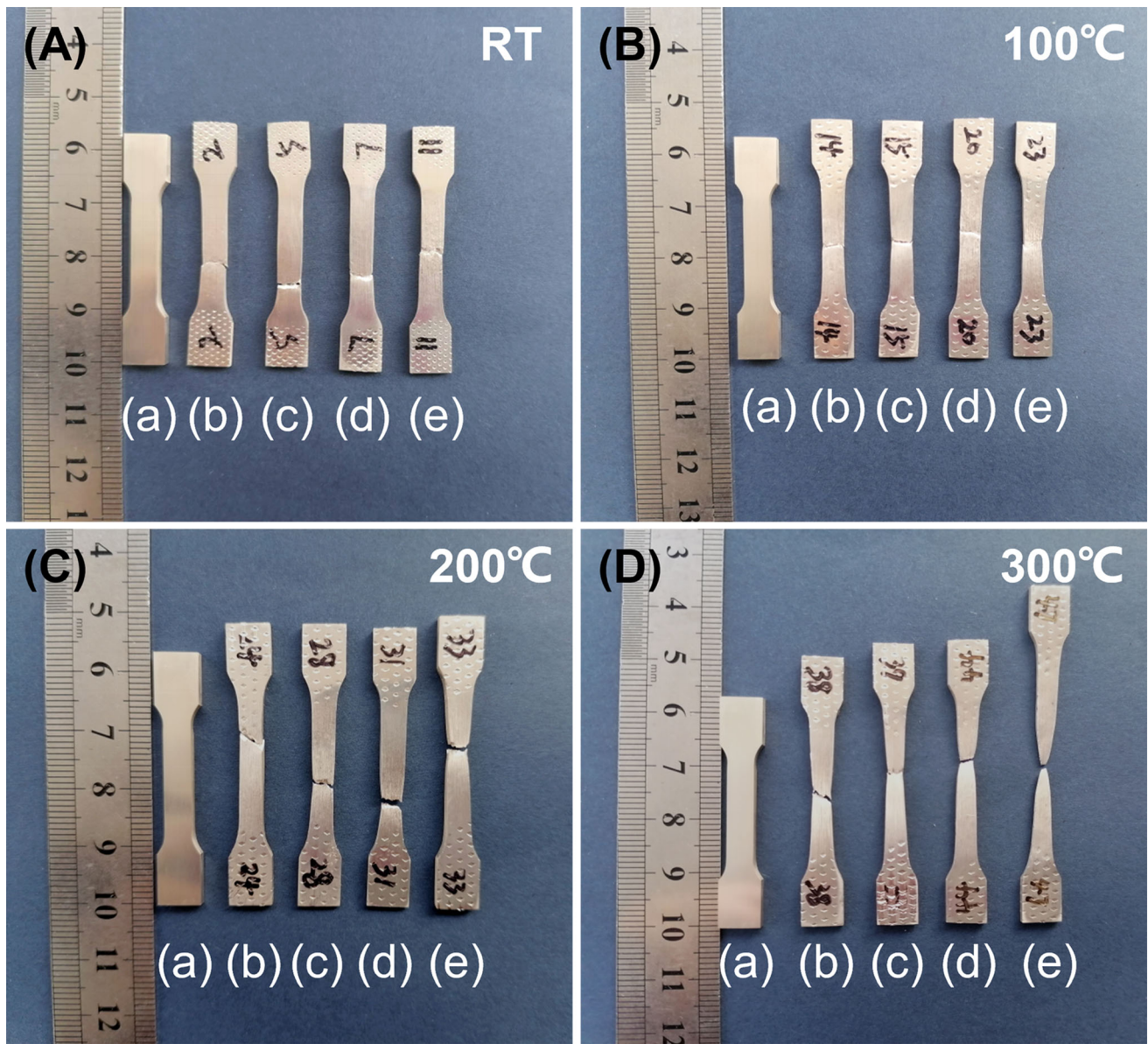
Fig. 9 Macroscopic morphology of tensile specimens of the extruded MYZN alloy before and after stretching at RT (A), 100 °C (B), 200 °C (C) and 300 °C (D) with different strain rates: (a) initial tensile specimen, (b-e) are typical specimens after fracturing with strain rates of 1×10^{-2} s^{-1}, 3×10^{-3} s^{-1}, 1×10^{-3} s^{-1} and 4×10^{-4} s^{-1}, respectively

Figures 10–12 show the surface and fracture morphology of tensile samples of the extruded MYZN alloy under at different strain rates from RT to 300 °C. It can be seen from the lateral surface of tensile samples at low magnification that the necking tendency increases with increasing temperature and decreasing strain rates. Also, the fracture and surface morphology of the alloy change at the above conditions; some slip lines/bands, microcracks and microvoids appear in lateral surface of the tensile samples. The microcracks occur at the interface between the second phase and α-Mg matrix and gradually expand into macrocracks parallel to tensile direction under the application

of external forces (Ref 29). This also leads to the release of stress concentration by the formation of these macrocracks in the extruded alloys, and the plasticity of the alloy can be improved effectively (Ref 30). With the decrease in strain rate, the microcracks gradually expand, aggregate and grow into larger macrocracks. It is noted that microvoids appear at 200 °C and 300 °C with low strain rates, suggesting that the grain boundary sliding and grain rotation take part in the plastic deformation as seen in Figs. 11(k) and 12(k). Moreover, the fracture of the extruded alloy mainly contains a large number of tearing edges and some shallow dimples with uneven distribu-
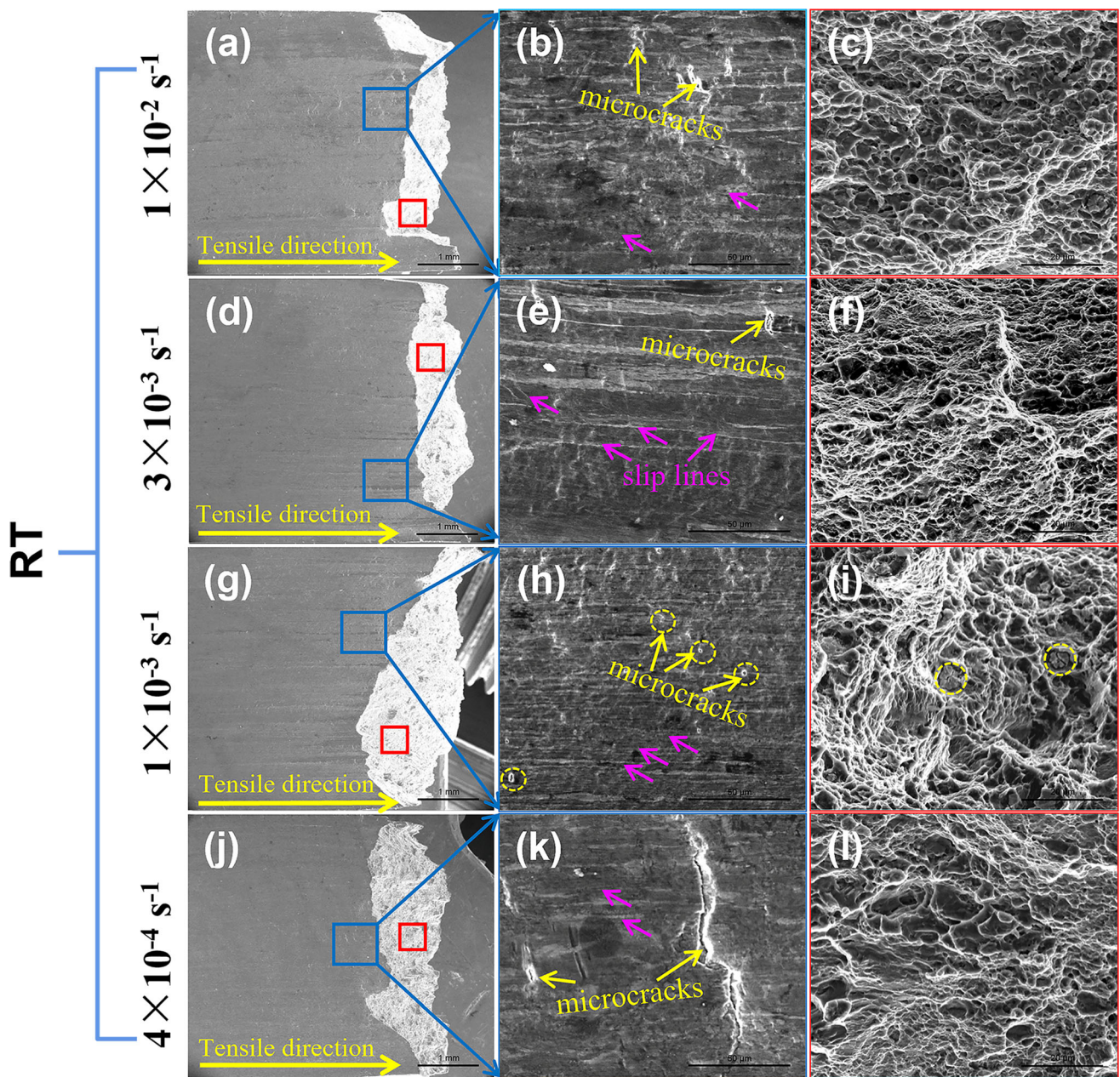
Fig. 10 The lateral surface (a, d, g, j) and fracture (c, f, i, l) of tensile samples of the extruded MYZN alloy at RT with different strain rates: 1×10^{-2} s^{-1} (a, b, c); 3×10^{-3} s^{-1} (d, e, f); 1×10^{-3} s^{-1} (g, h, i); and 4×10^{-4} s.$^{-1}$ (j, k, l)

tion at RT. The fracture morphology still remains at various strain rates as seen in Fig. 10. As increasing temperature and decreasing strain rate, the deep and even dimples are observed in the fracture of the alloy, especially at 300 °C with a strain rate of 4×10^{-4} s^{-1}. Some particles with cracks appear in the bottom of dimple as seen in Figs. 10(i), 11(c) and 12(c).

Figure 13 shows the microstructure of fracture regions of tensile samples for the extruded MYZN alloy at RT, 200 °C and 300 °C with strain rate of 1×10^{-2} s^{-1} and 4×10^{-4} s^{-1}, respectively. It can be seen that volume fraction of DRX regions generally increases, while that of non-DRX regions decreases with increasing temperature and decreasing strain

rate. This also results in the sufficient DRX of the extruded alloy at high temperatures and low strain rates. Also, the grain of the extruded alloy does not grow obviously even at 300 °C with a strain rate of 4×10^{-4} s^{-1}. Actually, the high-temperature resistant microstructures are mainly attributed to the block LPSO phase with a good thermal stability at the grain boundary, which effectively hinders grain boundary sliding and thus refines the grain during high-temperature deformation (Ref 11, 15). In addition, the microcavities can be observed at the interface between α-Mg matrix and LPSO phase and expand along the ED. The higher *m* value (0.17) at 300°C and the formation of these microcavities on the above surface
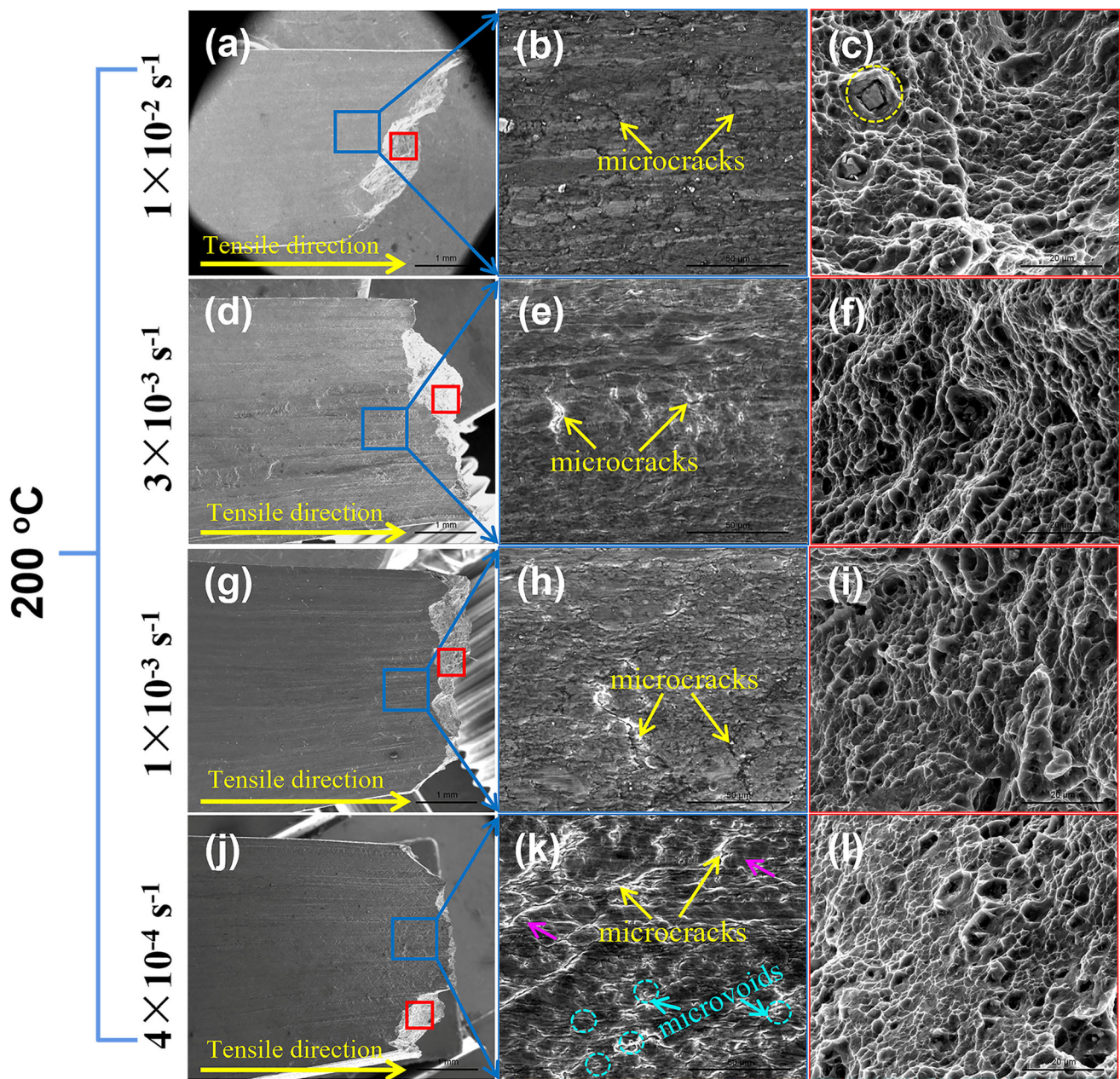
Fig. 11 The lateral surface (a, d, g, j) and fracture (c, f, i, l) of tensile samples of the extruded MYZN alloy at 200 °C with different strain rates: 1×10^{-2} s^{-1} (a, b, c); 3×10^{-3} s^{-1} (d, e, f); 1×10^{-3} s^{-1} (g, h, i); and 4×10^{-4} s.$^{-1}$ (j, k, l)

indicate that the grain boundary sliding dominates the deformation. In addition, the alloy exhibits a quasi-superplastic deformation behavior (ε_f = 130.3%) at 300 °C and $\dot{\varepsilon}$=4 × 10^{-4} s^{-1}. The superplasticity of the alloy is mainly due to the refinement and distribution of LPSO phase in the alloy during deformation, which could prevent grain from coarsening and thus facilitate superplastic deformation (Ref 31). Moreover, the grain boundary sliding can cause a local stress concentration at the interface between LPSO phase and Mg matrix, but the formation of microcavities could release the stress concentration, which is beneficial to improve the plasticity.

Figure 14 shows the bright-field TEM images of fracture regions of tensile samples for the extruded MYZN alloy at RT and 300 °C with a strain rate of 4×10^{-4} s^{-1}. As shown in Fig. 14(a) and (e), the typical sub-grains containing different dislocation configurations appear in the α-Mg matrix and some fine strip-like 14H-LPSO phases and SFs precipitate in the parts of sub-grains as seen Fig. 14(b) and (d). The HRTEM and FFT images in Fig. 14(c, d, g, h) indicate the dislocation densities of the matrix of the alloy at RT (1.7×10^{17}/m^2) are higher than that at 300 °C (9.5×10^{16}/m^2). With the increase in temperature, these dislocations cancel each other with those of opposite signs on the slip plane results in a reduction of
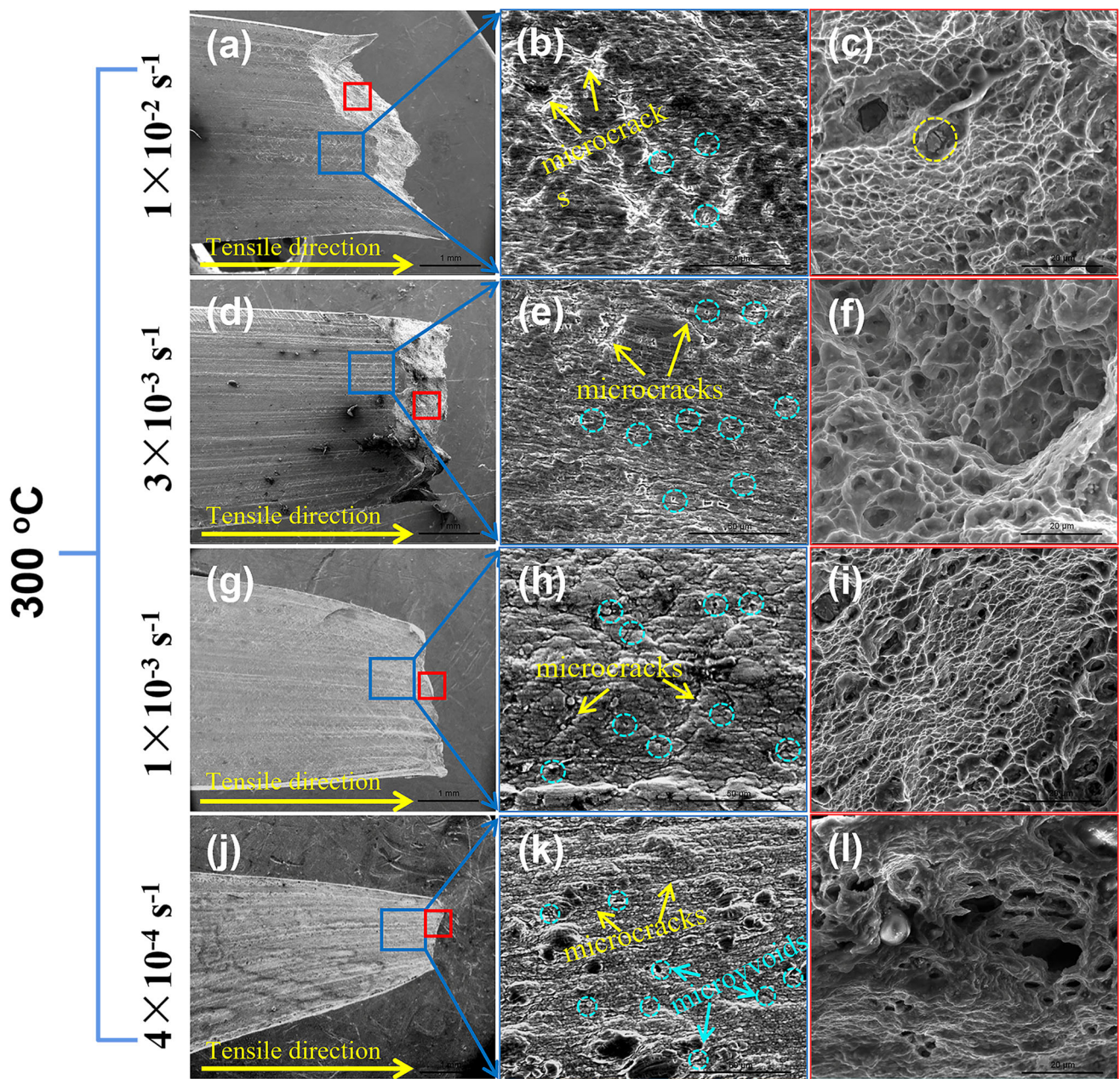
Fig. 12 The lateral surface (a, d, g, j) and fracture (c, f, i, l) of tensile samples of the extruded MYZN alloy at 300 °C with different strain rates: 1×10^{-2} s^{-1} (a, b, c); 3×10^{-3} s^{-1} (d, e, f); 1×10^{-3} s^{-1} (g, h, i); and 4×10^{-4} s.$^{-1}$ (j, k, l)

dislocation density. So, the strain softening caused by dislocation interaction and dislocation annihilation makes the tensile strengths of the extruded alloy decrease gradually with the increase in temperature. Furthermore, at high temperatures, the critical resolution shear stress (CRSS) of prismatic and pyramidal slip systems decreases, which also leads to the activation of non-basal slip systems. This is also the reason why the elongation of the extruded alloy increases significantly with the increase in temperature and decrease in strain rate.

4. Conclusions

(1) The extruded MYZN alloy is mainly composed of α-Mg, $Mg_{24}Y_5$, Mg_2Y, Y-rich phase and LPSO phase. Among them, LPSO phase has three morphologies: lamellar 18R- LPSO phase distributed along the ED,
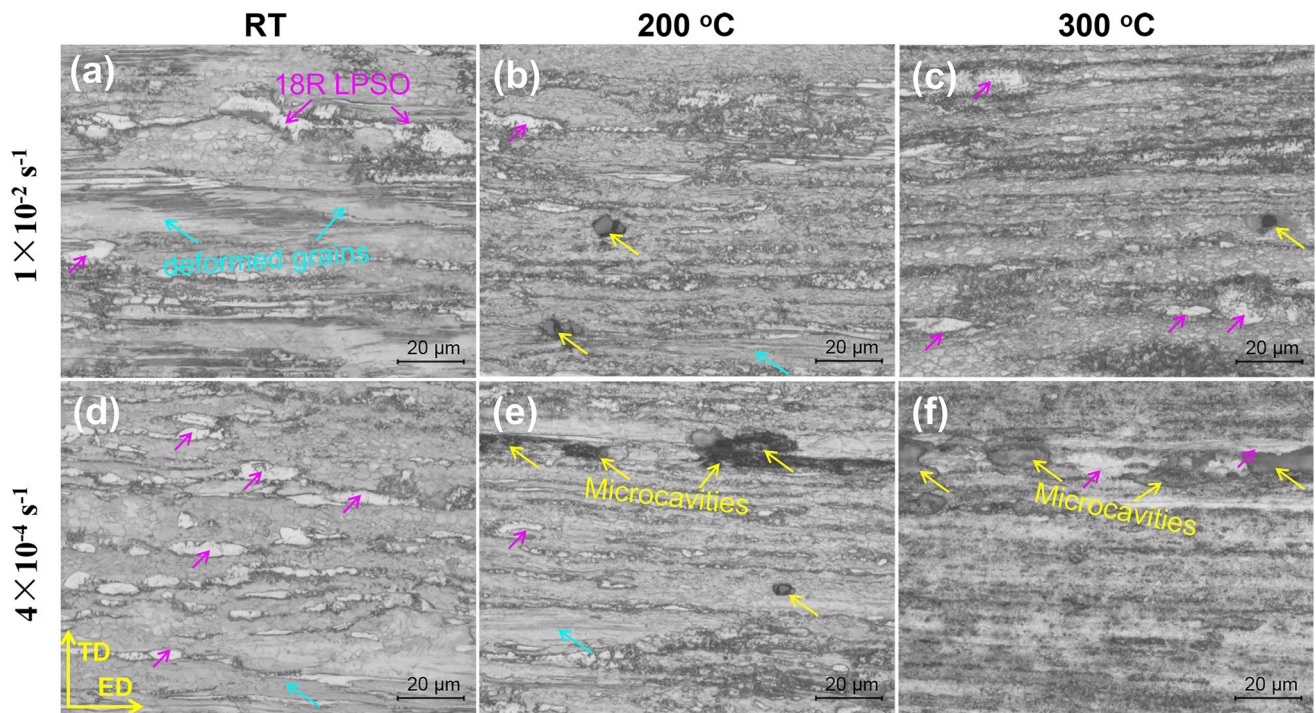
Fig. 13 Microstructures of fracture regions of tensile specimens for the extruded MYZN alloy at RT (a, d), 200 °C (b, e) and 300 °C (c, f) with strain rate of 1×10^{-2} s^{-1} (a, b, c) and 4×10^{-4} s^{-1} (d, e, f), respectively
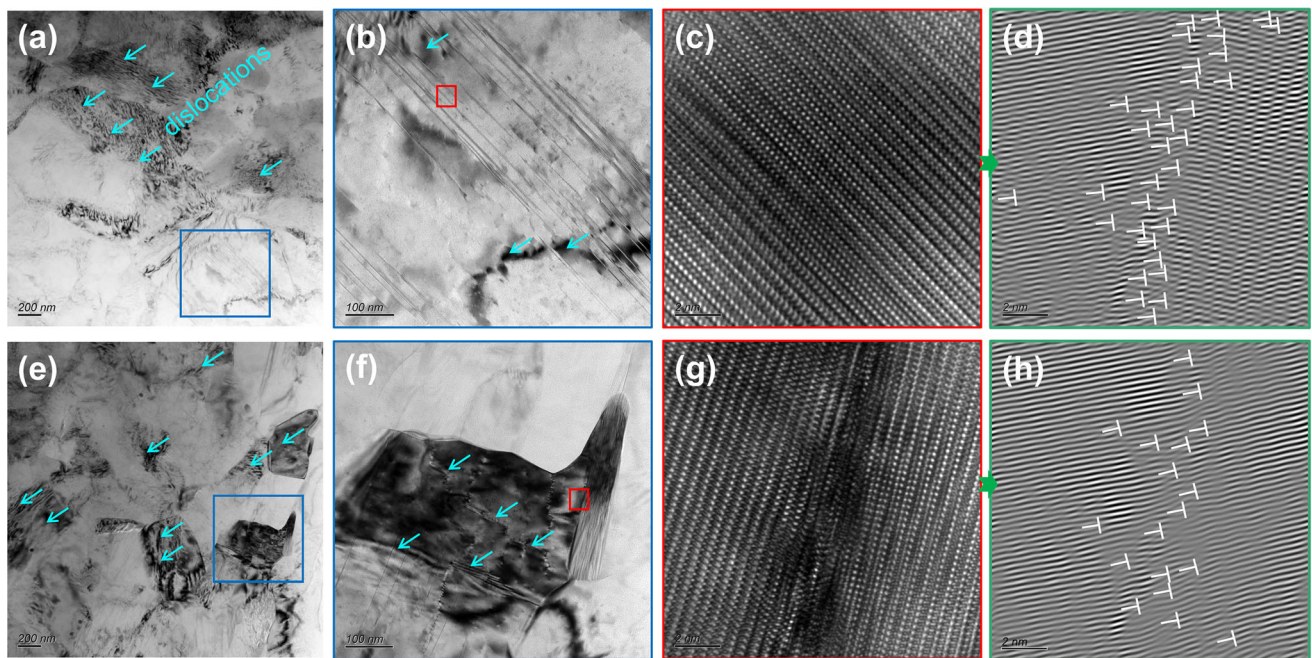

Fig. 14 The bright-field TEM images of the extruded MYZN alloy at RT (a, b, c d) and 300 °C (e, f, g, h) with a strain rate of 4×10^{-4} s^{-1}; (c) and (g) are HRTEM images of the red area in (b) and (f), (d) and (h) are corresponding FFT images of (c) and (g), respectively

block 18R-LPSO phase and thin strip 14H-LPSO phase and SFs in the grain interior.

(2) Tensile strengths of the extruded MYZN alloy decrease, while the elongation to failure gradually increases with the increase in temperature and the decrease in strain rate. At 300 °C and $\dot{\varepsilon} = 4 \times 10^{-4}$ s^{-1}, the elongation to

failure of the extruded MYZN alloy is up to 130.3%, which shows quasi-superplasticity. Based on surface observation of tensile specimens and the calculated m and Q values, the deformation of the extruded alloy is dislocation slipping at low temperatures with different

strain rates, while that does grain boundary sliding accompanied dislocation slipping at 300 °C.

(3) The hot processing map based on dynamic material model (DMM) shows Region II (247–300 °C/4×10^{-4}–1×10^{-3} s^{-1}) with high η values is identified as the suitable processing window for the extruded MYZN alloy.

References

1. J.H. Wang, L. Xu, R.Z. Wu, J. Feng, J.H. Zhang, L.G. Hou, and M.L. Zhang, Enhanced Electromagnetic Interference Shielding in a Duplex-Phase Mg-9Li-3Al-1Zn Alloy Processed by Accumulative Roll Bonding, *Acta Metall. Sin. (Engl. Lett.)*, 2020, **33**(4), p 490–499

2. J.S. Xie, Z. Zhang, S.J. Liu, J.H. Zhang, J. Wang, Y.Y. He, L.W. Lu, Y.L. Jiao, and R.Z. Wu, Designing New Low Alloyed Mg—RE Alloys with High Strength and Ductility Via High-Speed Extrusion, *Int. J. Miner. Metall. Mater.*, 2022, **30**(1), p 82–91

3. R.G. Li, H.J. Zhang, and G.Y. Fu, Microstructure and Mechanical Properties of Extruded Mg$_{96}$Zn$_1$Y$_3$ Alloy, *Mater. Charact.*, 2014, **98**, p 107–112

4. Z.H. Li, J.H. Zhang, Y. Feng, J.S. Xie, Y.F. Liu, S.J. Liu, J. Meng, Q. Yang, Z. Liu, and R.Z. Wu, Development of Hot-Extruded Mg-RE-Zn Alloy Bar with High Mechanical Properties, *Materials*, 2019, **12**(10), p 1722

5. F. Zhong, H.J. Wu, Y.L. Jiao, R.Z. Wu, J.H. Zhang, L.G. Hou, and M.L. Zhang, Effect of Y and Ce on the Microstructure, Mechanical Properties and Anisotropy of as-Rolled Mg-8Li-1Al Alloy, *J. Mater. Sci. Technol.*, 2020, **39**, p 124–134

6. J.H. Zhang, S.J. Liu, R.Z. Wu, L.G. Hou, and M.L. Zhang, Recent Developments in High-Strength Mg-RE-Based Alloys: Focusing on Mg-Gd and Mg-Y Systems, *J. Magnesium Alloys*, 2018, **6**(3), p 277–291

7. D. Wang, S.J. Liu, R.Z. Wu, S. Zhang, Y. Wang, H.J. Wu, J.H. Zhang, and L.G. Hou, Synergistically Improved Damping, Elastic Modulus and Mechanical Properties of Rolled Mg-8Li-4Y–2Er-2Zn-0.6Zr Alloy with Twins and Long-Period Stacking Ordered Phase, *J. Alloys Compd.*, 2021, **881**, p 160663

8. S.R. Zhang, J. Kim, F.X. Wang, K.K. Kang, H. Xue, X.H. Chen, and F.S. Pan, Microstructure and Mechanical Properties of LPSO Dominant Mg-2Y-Cu-TM (TM=Cu, Zn Co, Ni) Alloys, *Mater. Charact.*, 2022, **191**, 112111

9. K. Li, Z.Y. Chen, T. Chen, J.B. Shao, R.K. Wang, and C.M. Liu, Hot Deformation and Dynamic Recrystallization Behaviors of Mg-Gd-Zn Alloy with LPSO Phases, *J. Alloys Compd.*, 2019, **792**, p 894–906

10. S.Q. Luo, A. Tang, B. Jiang, H.W. Dong, W. Wei, and F.S. Pan, A High Strength and Toughness Mg-Y-Ni Alloy with a Long-Period Stacking Ordered Structure, *Mater. Sci. Forum*, 2017, **898**, p 172–178

11. G.L. Bi, Y.D. Li, X.F. Huang, T.J. Chen, J.S. Lian, Z.H. Jiang, Y. Ma, and Y. Hao, Deformation Behavior of an Extruded Mg-Dy-Zn Alloy with Long Period Stacking Ordered Phase, *Mater. Sci. Eng. A*, 2015, **622**, p 52–60

12. X.R. Zhang, G.X. Sun, W. Zai, Y. Jiang, Z.H. Jiang, S. Han, G.L. Bi, D.Q. Fang, and J.S. Lian, Effects of Temperature and Strain Rate on Deformation Behaviors of an Extruded Mg-5Zn-2.5Y-1Ce-0.5Mn Alloy, *Mater. Sci. Eng. A*, 2021, **799**, p 140141

13. X.D. Yang, X.J. Zhou, S.L. Yu, J. Zhang, X.Z. Lu, X.M. Chen, L.W. Lu, W.Y. Huang, and Y.R. Liu, Tensile Behavior at Various Temperatures of the Mg-Gd-Y-Zn-Zr Alloys with Different Initial Morphologies of LPSO Phases Prior to Extrusion, *Mater. Sci. Eng. A*, 2022, **851**, p 143634

14. X.Z. Jin, W.C. Xu, D.B. Shan, C. Liu, and Q. Zhang, Deformation Behavior, Microstructure Evolution and Hot Workability of Mg-37Gd-29Y-0.7Zn-07Zr alloy, *Met. Mater. Int.*, 2017, **23**(3), p 434–443

15. X.J. Zhou, Y. Yao, J. Zhang, X.Z. Lu, K. Xu, H. Liu, and Z.J. Wu, Improved Workability for Mg-Y-Zn Alloys Via Increased Volume Fraction of Block LPSO Phases, *Mater. Sci. Eng. A*, 2020, **794**, p 139934

16. G.L. Bi, Y.S. Wang, J. Jiang, J.R. Gu, Y.D. Li, T.J. Chen, and Y. Ma, Microstructure and Mechanical Properties of Extruded Mg-Y-Zn (Ni) Alloys, *J. Alloys Compd.*, 2021, **881**, p 160577

17. D.X. Zhang, Z. Tan, Q.H. Huo, Z.Y. Xiao, Z.W. Fang, and X.Y. Yang, Dynamic Recrystallization Behaviors of Mg-Gd-Y-Zn-Zr Alloy with Different Morphologies and Distributions of LPSO Phases, *Mater. Sci. Eng. A*, 2018, **715**, p 389–403

18. T. Chen, Z.Y. Chen, J.B. Shao, Y.X. Han, L.H. Mao, and C.M. Liu, Fragmentation of Long Period Stacking Ordered (LPSO) Phase and Its Impact on Microstructure Evolution of a Mg-Y-Zn Alloy During Multi-Directional Forging, *Mater. Sci. Eng. A*, 2020, **793**, p 139898

19. H. Liu, J. Ju, X.W. Yang, J.L. Yan, D. Song, J.H. Jiang, and A.B. Ma, A Two-Step Dynamic Recrystallization Induced by LPSO Phases and Its Impact on Mechanical Property of Severe Plastic Deformation Processed Mg$_{97}$Y$_2$Zn$_1$ Alloy, *J. Alloys Compd.*, 2017, **704**, p 509–517

20. V. Jain and R.S. Mishra, Gouthama, Superplastic Behavior and Microstructural Stability of Friction Stir Processed AZ91C Alloy, *J. Mater. Sci.*, 2013, **48**(6), p 2635–2646

21. R. Alizadeh, R. Mahmudi, A.H.W. Ngan, Y. Huang, and T.G. Langdon, Superplasticity of a Nano-Grained Mg-Gd-Y-Zr Alloy Processed by High-Pressure Torsion, *Mater. Sci. Eng. A*, 2016, **651**, p 786–794

22. T.Y. Kwak and W.J. Kim, Superplastic Behavior of an Ultrafine-Grained Mg-13Zn-1.55Y Alloy with a High Volume Fraction of Icosahedral Phases Prepared by High-Ratio Differential Speed Rolling, *J. Mater. Sci. Technol.*, 2017, **33**(9), p 919–925

23. T.G. Langdon, A Unified Approach to Grain Boundary Sliding in Creep and Superplasticity, *Acta Metall. Mater.*, 1994, **42**(7), p 2437–2443

24. D.D. Zhang, K. Guan, Q. Yang, B. Jiang, C. Sun, N. Wang, B.S. Li, D.P Zhang, X.L. Li, X.J. Liu, Z.Y. Cao, and J. Meng, Microstructures, Mechanical Properties and Creep Behavior of a Mg-3Yb-0.6Zn-0.4Zr Casting Alloy, *Mater. Sci. Eng. A*, 2019, **745**, p 360–368

25. L. Zhang, J.H. Zhang, C. Xu, S.J. Liu, Y.F. Jiao, L.J. Xu, Y.B. Wang, J. Meng, R.Z. Wu, and M.L. Zhang, Investigation of High-Strength and Superplastic Mg-Y-Gd-Zn Alloy, *Mater. Des.*, 2014, **61**, p 168–176

26. H.Y. Wu, C.T. Wu, J.C. Yang, and M.J. Lin, Hot Workability Analysis of AZ61 Mg Alloys with Processing Maps, *Mater. Sci. Eng. A*, 2014, **607**, p 261–268

27. R.K. Gupta, S.V.S. Narayana Murty, B. Pant, V. Agarwala, and P.P. Sinha, Hot workability of $\gamma+\alpha2$ Titanium Aluminide: Development of Processing Map and Constitutive Equations, *Mater. Sci. Eng. A*, 2012, **551**, p 169–186

28. Z. Jia, L.D. Yu, B.L. Wei, X. Sun, Y.J. Wang, D.X. Liu, and Y.T. Ding, High-Temperature Thermal Deformation Behavior and Microstructural Evolution of Inconel 617 Alloy, *Rare Met. Mater. Eng.*, 2022, **51**(2), p 461–468

29. G.L. Bi, Y.X. Han, J. Jiang, Y.D. Li, D.Y. Zhang, D. Qiu, and M. Easton, Microstructure and Mechanical Properties of an Extruded Mg-Dy-Ni Alloy, *Mater. Sci. Eng. A*, 2019, **760**, p 246–257

30. M. Okayasu, S. Takeuchi, M. Matsushita, N. Tada, M. Yamasaki, and Y. Kawamura, Mechanical Properties and Failure Characteristics of Cast and Extruded Mg$_{97}$Y$_2$Zn$_1$ Alloys with LPSO Phase, *Mater. Sci. Eng. A*, 2016, **652**, p 14–29

31. Z. Leng, J.H. Zhang, H.Y. Lin, P.F. Fei, L. Zhang, S.J. Liu, M.L. Zhang, and R.Z. Wu, Superplastic Behavior of Extruded Mg-9RY-4Zn Alloy Containing Long Period Stacking Ordered Phase, *Mater. Sci. Eng. A*, 2013, **576**, p 202–206